Fig. 4 Measured probe descent module spin performance compared with a posteriori spin assessment. Two sets of numbers correspond to descent time and spin rate in the first and last data acquisition intervals.

spin response. This assessment was derived from further model calculations based on drop and wind-tunnel tests.

Five minutes past entry, the spin rate was measured as ±33 rpm (33.48 rpm at 4.9 min). A cursory comparison with Fig. 3 suggests that the spin direction at aeroshell jettison was positive, i.e., not reversed by ablative grooving, although insufficient data during this initial descent period exist to conclude this with certainty. Ancillary data, however, confirm that the intent of the transient spin requirement was adequately met. Because the Orbiter-mounted relay radio receivers managed to lock onto the probe's modulated signal much sooner than expected (~35 s instead of the specified 1-min maximum), it is clear that any high-rate probe spin that might have been induced by entry forces was quickly damped. If this were not the case, the phase error of the received signal—predominantly due to spinning effects during initial signal acquisition—would have been too high to permit rapid signal acquisition.[9]

For the remainder of the descent mission, the spin assessment appears to provide a more conservative, lower-bound spin estimate, matching the flight data to within about 5 rpm. However, the assessment itself is based on an equation of motion, which assumed that the parachute was nonspinning and, hence, would not be expected to accurately replicate the actual flight condition of a spinning parachute/spinning DSM whose composite rolling moment and roll damping coefficients were never measured or analyzed. Furthermore, the assessment ignored the possibility of dynamic coupling of pitch and yaw disturbances into the probe spin. Again, this was because aerodynamic test and design efforts were focused toward meeting the transient spin requirement. For the balance of the descent mission (beyond 5 min past entry), it was always deemed sufficient that the probe simply have a nonzero spin. (It is interesting to note that the terminal spin rate measured during the aforementioned test in Earth's atmosphere was within 4% of the final Jovian spin measurement.) The last point recorded, at 50.77 min after entry, corresponded to a spin of 14.2 rpm.

Conclusions

The comparison of the measured probe descent spin with the calculated spin assessment, as well as the excellent acquisition of the communications link to the Orbiter, show that the aerodynamic spin design of the probe was entirely adequate. The spin was slow enough to provide favorable conditions for timely establishment of a communications link with the overflying Orbiter and fast enough to provide the science payload sensors a continuous 360-deg survey of the local horizon throughout the Jovian descent mission.

Acknowledgments

tems Company—Homer H. Schwartz III and Telford W. Oswald (retired)—is readily acknowledged.

References

[1]Lanzerotti, L. J., Rinnert, K., Dehmel, G., Gliem, F. O., Krider, E. P., Uman, M. A., Umlauft, G., and Bach, J., "The Lightning and Radio Emission Detector (LRD) Instrument," Space Science Reviews, Vol. 60, Nos. 1–4, 1992, pp. 91–109.

[2]Oswald, T. W., "Spin Vane Angles for Descent Module," Missile Systems Group, Hughes Aircraft Co., Hughes IDC HS373-3131, Canoga Park, CA, Aug. 1983.

[3]"Probe System and Related Requirements," Galileo Probe Project, NASA Ames Research Center, ARC Specification JP 510.00 (Rev. 4), Moffett Field, CA, Feb. 1982.

[4]Oswald, T. W., "Galileo Probe Descent Module Aerodynamics Final Report," Missile Systems Group, Hughes Aircraft Co., Hughes IDC HS373-3190, Canoga Park, CA, Oct. 1983.

[5]Rubin, L., "Spin Vane Angle Tolerance," Missile Systems Group, Hughes Aircraft Co., Hughes IDC HS373-4335, El Segundo, CA, Nov. 1988.

[6]Kim, V., "Spin Vane Angle Verification," Space and Communications Group, Hughes Aircraft Co., Hughes TSS V095, El Segundo, CA, April 1989.

[7]Radecki, J. T., "Pre Ship Viewgraph Book: Descent Module Aerodynamics," Space and Communications Group, Hughes Aircraft Co., Hughes IDC HS373-3297, El Segundo, CA, Feb. 1984.

[8]Talley, R. G., "Galileo Probe Deceleration Module Final Report," Re-Entry Systems Operations, General Electric Co., Document 84SDS2020, Philadelphia, PA, Jan. 1984.

[9]Neff, J. M. (ed.), "Galileo Probe-Orbiter Relay Link Integration Report: Figure 4.3-6, Phase Error Contributions to PLL Due to Environmental Effects," JPL D-1038(C)/NASA 1625-145(C), Pasadena, CA, Oct. 1994.

J. D. Gamble
Associate Editor

Flowfield over Bulbous Heat Shield in Transonic and Low Supersonic Speeds

R. C. Mehta*
Vikram Sarabhai Space Center,
Trivandrum 695022, India

Nomenclature

C_p	= pressure coefficient
D	= maximum payload shroud diameter, m
d	= booster diameter, m
e	= specific energy, J/kg
F	= vector of x-directed fluxes
G	= vector of r-directed fluxes
H	= source vector
M	= Mach number
p	= static pressure, N/m^2
q	= heat flux, W/m^2
Re	= Reynolds number
t	= time, s
U	= conservative variables in vector form
u, v	= velocity components, m/s
x, r	= coordinate directions, m
ρ	= density, kg/m^3
σ	= stress vector, N/m^2

*Engineer, Aerodynamics Division. Senior Member AIAA.

Introduction

A BULBOUS payload shroud is generally employed to accommodate an increase in payload volume of the satellite in a launch vehicle. A complex flowfield is observed around such a configuration due to the formation of a terminal shock, its interaction with the turbulent boundary layer, and flow separation in the boat-tail region during ascent flight in the transonic-speed range. The boundary layer in the boat-tail region is considerably thicker; therefore, the evaluation of viscous–inviscid interaction becomes necessary. Assessment of the separation region and knowledge of the surface pressure distribution are required for acoustic insulation design purposes.

A literature survey shows that experimental and numerical efforts have been made to analyze the complex fluid mechanics of the bulbous payload shroud of a launch vehicle. Experimental investigations were limited to the measurement of surface pressure distribution and oil flow patterns.[1,2] Numerical simulations have been performed to examine the shock/turbulent boundary-layer interaction and separated flow region in the vicinity of the boat-tail region.[3,4] For the various heat shield geometries, the available data are not sufficient to determine the movement of the terminal shock, the shock-induced separated flow on the forebody cylinder, and the separated flow caused by the boat tail.

The present work employs a computational fluid dynamics approach to analyze such a complex fluid dynamics problem. The time-dependent, compressible, turbulent Reynolds-averaged Navier–Stokes equations are solved using a finite volume discretization in conjunction with a three-stage Runge–Kutta time-stepping scheme. The main purpose of the present numerical simulation is to study the formation of the terminal shock and its movement over the forebody cylinder in the transonic Mach number range. The behavior of the separated flow in the boat-tail region is also investigated in the Mach number range $0.8 \leq M \leq 3.0$ and Reynolds number range 3.314×10^7–4.682×10^7/m. A comparison is made with the experimental results obtained from the wind tunnel.

Governing Equations and Numerical Scheme

The axisymmetric, compressible, turbulent, Reynolds-averaged Navier–Stokes equations can be written as

$$\frac{\partial U}{\partial t} + \frac{\partial F}{\partial x} + \frac{1}{r}\frac{\partial (rG)}{\partial r} = \frac{H}{r} \tag{1}$$

where

$$U = [\rho, \rho u, \rho v, \rho e]^T$$

$$F = \left[\rho u, \rho u^2 - \sigma_{xx}, \rho u v - \sigma_{xr}, (\rho e - \sigma_{xx})u - \sigma_{xr}v + q_x\right]^T$$

$$G = \left[\rho v, \rho u v - \sigma_{xr}, \rho v^2 - \sigma_{rr}, (\rho e - \sigma_{rr})v - \sigma_{rx}u + q_r\right]^T$$

$$H = [0, 0, \sigma_+, 0]^T$$

Reynolds stress and turbulent heat fluxes are modeled by introducing an isotropic eddy viscosity term. The coefficient of molecular viscosity is calculated according to Sutherland's law. The closure of the system of equations is achieved by introducing the Baldwin–Lomax turbulence model.[5] The temperature is related to pressure and density by the perfect-gas equation of state.

The numerical algorithm employs a finite volume discretization technique. The computational domain is divided into a number of quadrilateral cells. The integral conservation equations are applied to each computational cell in turn. The convective fluxes are calculated at the center of the cell, whereas the viscous fluxes are defined at the vertices of the cell.[6] A system of ordinary differential equations in time is obtained after summing the flux vectors on each face of the cell. Temporal integration is performed using the multistage time-stepping method.[7] Further details of the numerical procedure are given in Ref. 8.

Four different types of boundary conditions are required for the computation of the flowfield, i.e., inflow, solid wall, outflow, and centerline conditions. At the inflow, all of the flow variables are prescribed at freestream conditions. On the heat shield wall, the no-
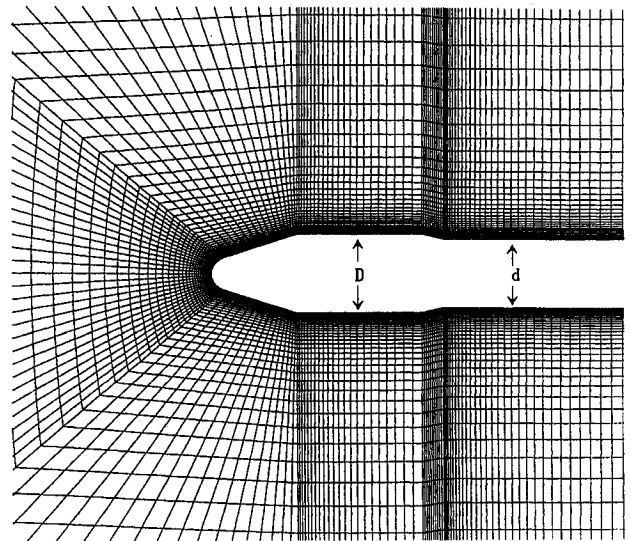

Fig. 1 Enlarged view of grid.

slip and isothermal wall conditions are considered. For the subsonic flow, nonreflecting far-field boundary conditions are applied at the outer boundary of the computational domain. For supersonic flow, all of the flow variables are extrapolated at the outflow from the vector of conserved variables U. At the line of symmetry, ahead of the heat shield, an image cell is imposed on the solved variables.

The aforementioned numerical procedure is employed to obtain the flowfield along a typical bulbous payload shroud. The maximum payload shroud diameter of the model is 0.04 m, whereas the booster diameter is 0.035 m. The boat-tail angle is 15 deg measured clockwise from the axis with reference to the oncoming flow direction. For the blunt-nosed cone, the inclination at the forebody junction is 20 deg and the total length of the shroud from the stagnation point to the boat tail is 0.083 m. These subscale dimensions were chosen after considering the blockage and compatibility conditions with the model system support of the wind tunnel.[1,9] Grid-independent tests and the convergence criterion are discussed in Ref. 8. The computation is performed using 132×62 grid points. Figure 1 shows an enlarged view of the grid.

Results and Discussion

The current experimental data consist of schlieren photographs and surface pressure distributions.[9,10] The flowfield and resulting wall pressure distributions are computed for the freestream Mach number range $0.8 \leq M \leq 3.0$ and Reynolds number range 3.314×10^7–4.682×10^7/m based on the wind-tunnel test conditions.[9] Figure 2 shows the comparison between the density contour plots and schlieren photographs for $M = 0.8$ and 0.9. It can be observed from Fig. 2 that all of the essential flowfield features of the transonic flow, such as supersonic pocket, terminal shock, and expansion and compression regions, are very well captured and compare well with the schlieren photographs. The terminal shock just reaches the end of the forebody cylinder at $M = 0.95$, as shown in Ref. 8. The density contour plots reveal that the supersonic region increases with increasing freestream Mach number, and as a result, the terminal shock moves downstream with increasing freestream Mach number. Comparison between the shock locations of the numerical and experimental results is shown in Fig. 3. It can be seen that the terminal shock crosses the forebody cylinder at about $M = 0.97$. The location of the terminal shock is found to be a nonlinear function of Mach number.

In recent numerical studies,[8] a local flow separation is observed in the boat-tail region and is found to be a function of Mach number. A schematic sketch of the separated flow in the boat-tail region at the transonic and supersonic Mach numbers, which are reconstructed from the velocity vector[8] and density contour plots, is shown in Fig. 4. For the transonic case, a shear layer is formed, and it contains a recirculating region as shown in Fig. 4a. The downstream boundary layer is found to be thick, which is nearly the boat-tail
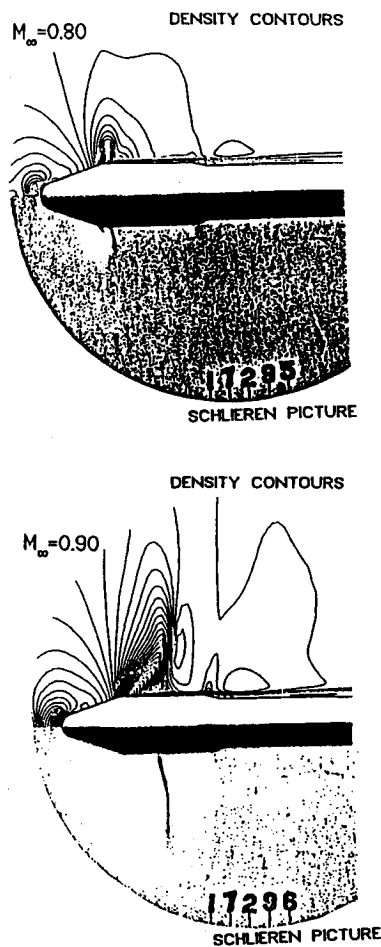
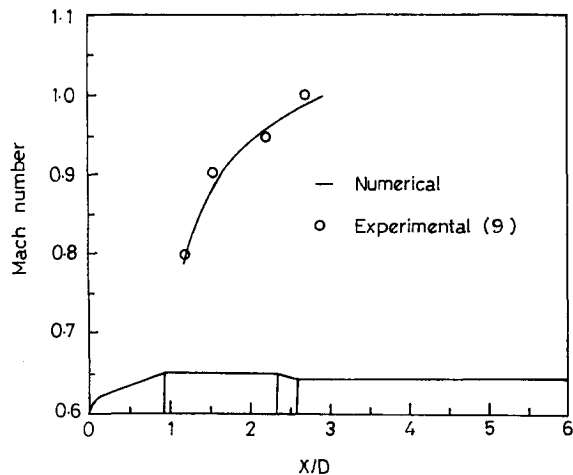Fig. 2   Comparison between density contours and schlieren picture.

Fig. 3   Shock location at various freestream Mach numbers.

height. Figure 4b shows flowfield features for the supersonic case. The flow turns downstream of the boat tail through an expansion fan with a resulting mixing layer that separates the supersonic fluid above the subsonic recirculating region below it. The pressure in the recirculating region is generally uniform and below that of the freestream pressure. As the mixing layer impinges on the downstream wall, the flow turns back toward the freestream direction and a recompression shock wave is typically formed.

The surface pressure coefficient C_p vs nondimensional length x/D of the heat shield for various values of freestream Mach numbers is presented in Figs. 5 and 6. In the case of the transonic-speed range, the computed results compare well with the experimental results along the entire length of the shroud except at the cone–cylinder junction in the transonic range, where the maximum expansion occurs. Near the stagnation point and on the spherical region, a steep
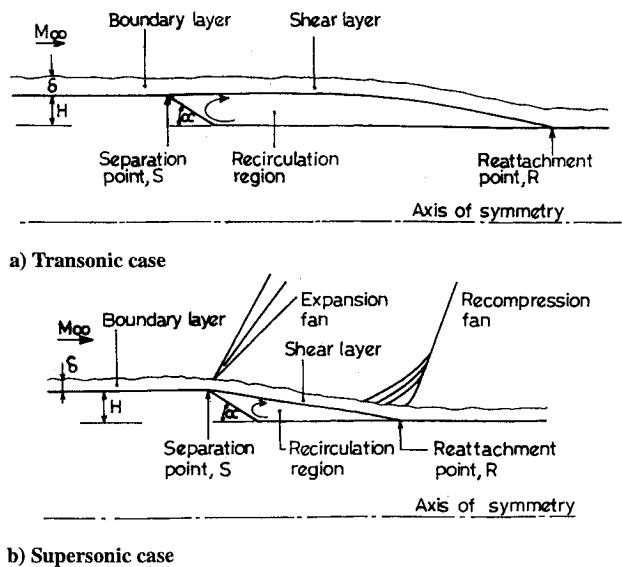

a) Transonic case

b) Supersonic case

Fig. 4   High-speed flow over boat-tail region.
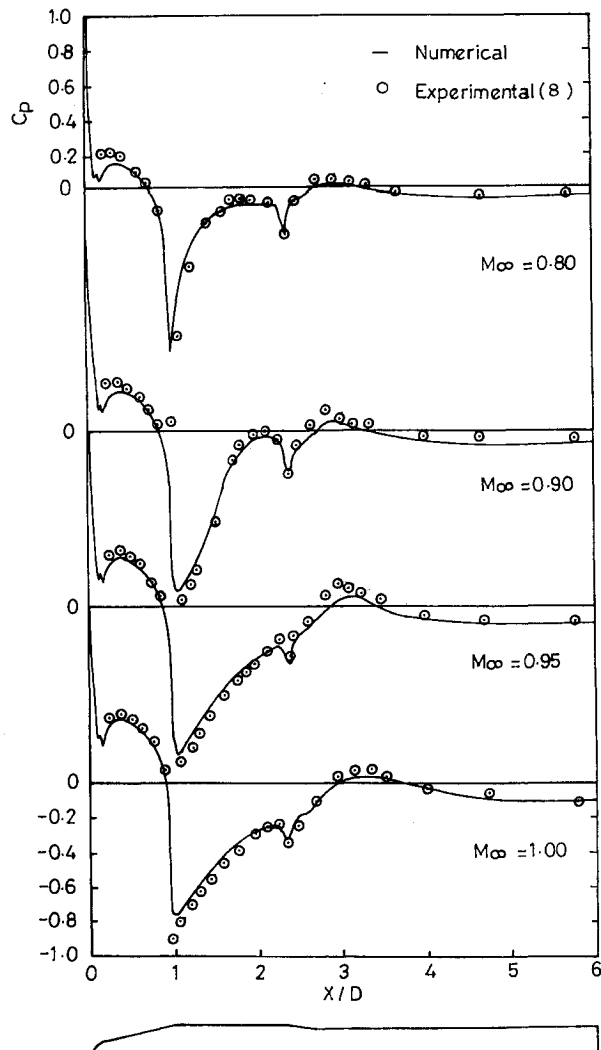

Fig. 5   Pressure distribution along heat shield; $M \leq 1.0$.

fall in the pressure coefficient was noticed, which is partially recovered along the cone. The experimental values also agree with this trend from the station $x/D = 0.22$ onward, where the first pressure measurement was made. On the forebody cylinder, the pressure distribution pattern also confirms the movement of the terminal shock, as observed in the density contour plots. In the boat-tail region, the expansions and compressions are comparatively mild. In the case of the supersonic Mach number range, the expansion at the cone
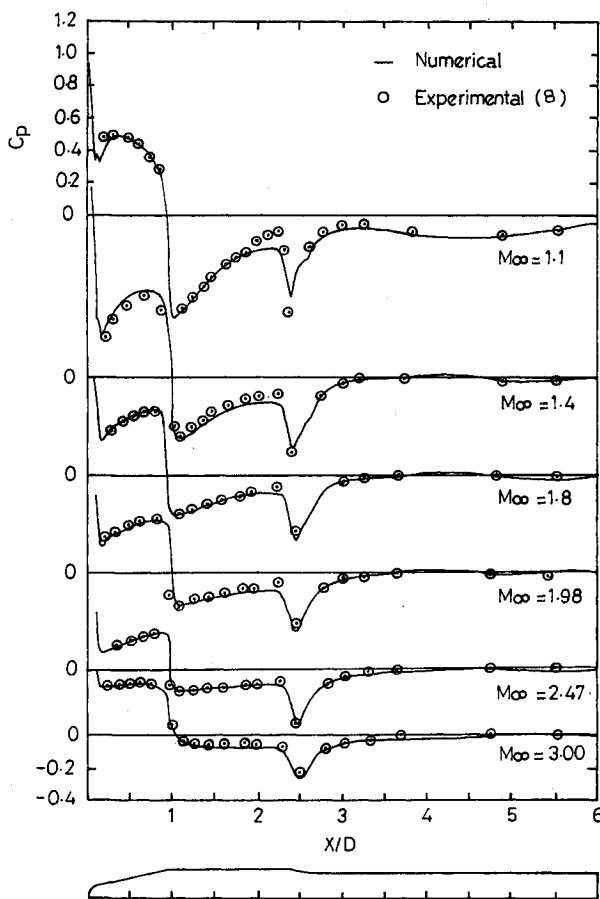
Fig. 6   Pressure distribution along heat shield; $M \leq 3.0$.

forebody and the boat-tail region reduces with increasing supersonic Mach number.

Conclusions

A numerical experiment of axisymmetric turbulent viscous flow over a bulbous heat shield is performed by employing a three-stage Runge–Kutta time-stepping scheme. Turbulence closure is achieved using the Baldwin–Lomax turbulence model. The flowfield visualization of the terminal shock and the separated region helps in a systematic understanding of flow structure under various freestream Mach numbers. The following observations are made based on the described numerical simulations.

1) The terminal shock moves downstream with increasing freestream Mach number. The strength of the terminal shock initially increases with Mach number and later decreases. The location of the terminal shock is found as a nonlinear function of the freestream Mach number.

2) The separation zone in the boat-tail region is found as a function of the freestream Mach number. The flowfield features of the separated region are found to be different in the transonic and supersonic Mach number ranges.

References

[1]Ahmed, S., and Selvarajan, S., "Investigation of Flow on a Hammerhead Nose Configuration at Transonic Speeds," AIAA Paper 91-1711, June 1991.

[2]Ramaswamy, M. A., and Rajendra, G., "Experimental Investigation of Transonic Flow Past a Blunt Cone–Cylinder," *Journal of Spacecraft and Rockets*, Vol. 15, No. 2, 1978, pp. 120–123.

[3]Purohit, S. C., "A Navier–Stokes Solution for a Bulbous Payload Shroud," *Journal of Spacecraft and Rockets*, Vol. 23, No. 6, 1986, pp. 590–596.

[4]Deese, J. E., Gielda, T. J., Agarwal, R. K., and Pavish, D. J., "Prediction of Flow Separation on Launch Vehicle Configuration," AIAA Paper 91-1727, June 1991.

[5]Baldwin, B. S., and Lomax, H., "Thin Layer Approximation and Algebraic Model for Separated Turbulent Flow," AIAA Paper 78-257, Jan. 1978.

[6]Peyret, R., and Vivind, H., *Computational Methods for Fluid Flow*, Springer–Verlag, Berlin, 1993, pp. 109–111.

[7]Jameson, A., Schmidt, W., and Turkel, E., "Numerical Solution of Euler Equations by Finite Volume Methods Using Runge–Kutta Time Stepping Schemes," AIAA Paper 81-1259, 1981.

[8]Mehta, R. C., "Transonic Flow Simulation for a Bulbous Heat Shield," *Journal of Spacecraft and Rockets*, Vol. 34, No. 4, 1997, pp. 561–564.

[9]Prasad, J. K., Varambally, B. S., and Pillai, N. M., "Aerodynamic Load on Heat Shield in Mach Number Range of 0.8 to 1.1," Vikram Sarabhai Space Center, AFDG:01:84, Trivandrum, India, June 1984.

[10]Ahmed, S., "Flow Visualization Studies at Transonic Speeds on Heat Shield Configurations," National Aeronautical Labs., NAL-TWT-1-36, Bangalore, India, July 1984.

J. R. Maus
Associate Editor

Euler Solution of Axisymmetric Jets in Supersonic External Flow

Erdal Yılmaz* and Mehmet Şerif Kavsaoğlu†
Middle East Technical University,
06531 Ankara, Turkey

Nomenclature

a	= speed of sound, m/s
D	= nozzle external diameter, m
F	= convective flux vector in x direction, nondimensional
G	= convective flux vector in y direction, nondimensional
H^*	= axisymmetric source vector, nondimensional
K	= node number, nondimensional
M	= Mach number, nondimensional
P	= pressure, nondimensionalized with P_∞
R	= residual, nondimensional/radius, m
r	= radial distance, m
S	= control volume surface, nondimensionalized with D^2
t	= time, nondimensionalized with a_∞ and D
U	= solution vector, nondimensional
V	= velocity vector, nondimensionalized with a_∞
x, y	= two-dimensional or axially symmetric coordinates, nondimensionalized with D
γ	= ratio of specific heats, nondimensional
Ω	= control volume, nondimensionalized with D^3

Subscripts

j	= jet
∞	= infinity

Introduction

AN exhaust plume expansion into a supersonic external freestream is a complex phenomenon. The plume boundary behaves as a curved rigid body, and it causes a curved shock wave. Very large gradients exist around these regions.[1] Some experimental studies have been performed to obtain plume behavior at different jet exit pressure ratios.[2–4] There are several methods for predicting exhaust plume boundaries.[1,2,5,6]

In this study, axisymmetric Euler equations were solved by using a finite volume technique on unstructured triangular grids. Jet plume boundaries and other flowfield details were obtained for supersonic axisymmetric jets in a parallel supersonic external flow. The jet-to-freestream pressure ratio varied between 1 and 1500. For very high pressure ratios, computations are started with a low pressure ratio,

*Ph.D. Student, Aeronautical Engineering Department.
†Associate Professor, Aeronautical Engineering Department. Senior Member AIAA.